The volatile composition of Comet C/2017 E4 (Lovejoy) before its disruption, as revealed by high-resolution infrared spectroscopy with iSHELL at the NASA-IRTF.

Faggi S., Villanueva G. L., Mumma M. J., Paganini L.

Abstract

In April 2017, we acquired comprehensive high-resolution spectra of newly-discovered comet C/2017 E4 (Lovejoy) as it approached perihelion, and before its disintegration. We detected many cometary emission lines in the $(2.8 - 5.3)$ μm range, in four customized instrument settings (L1-c, L3, Lp1-c and M1) of iSHELL - the new near-IR high resolution immersion echelle spectrograph at NASA/IRTF (Maunakea, Hawaii). We identified twelve molecular species; nine primary volatiles (H_2O, HCN, NH_3, CO, C_2H_2, C_2H_6, CH_4, CH_3OH, H_2CO) and three product species (CN, NH_2, OH). We detected 85 H_2O emission lines from 12 water vibrational bands across L1-c and M1 settings. The many detected water emission lines enabled retrieval of accurate measures for ortho- and para-H_2O independently, thereby reducing systematic uncertainty in the derived ortho-para ratio and nuclear spin temperature. Excitation analyses and emission profile analyses were performed for all species, and molecular abundance ratios relative to water are compared with values found for other Oort Cloud comets in our infrared database. Abundance ratios are consistent for most species, with the exception of under-abundant methanol and over-abundant ammonia in E4.

1. Introduction

Cosmogonic indicators in comets may preserve information on formative processes in the early solar nebula during the accretion of cometary ices and their later influence on young planets. Our knowledge about such infant stages of our proto-planetary system is still fragmentary and cometary nuclei retain the least processed material from that era – some may retain pristine material from the natal interstellar cloud core. Thus, investigations of cometary composition and the associated cosmogonic indicators are essential for testing models of Solar System formation and evolution, for assessing cometary delivery of organic compounds to the early Earth, and for addressing the origin of water on Earth and other terrestrial planets.

The retrieval of cosmogonic indicators has been targeted for decades, with progress advancing regularly as state-of-the-art instruments and spectroscopic analysis have matured. The principal targets are: isotopic ratios (isotopic enrichment is sensitive to the primordial conditions in which molecules formed), spin isomeric ratios (they may preserve information on the molecular formation temperature), and molecular abundances (they are strongly influenced by both local and large-scale diversity in chemical and physical processes during the formative phase of the protoplanetary disk).

 The 1986 apparition of comet 1P/Halley marked a major watershed for such studies, bringing the first accurate measurements of isotopic ratios in cometary water (D/H and $^{18}O/^{16}O$) and in radical CN ($^{13}C/^{12}C$) (Eberhardt et al. 1995; Jessberger et al. 1988), the first detection of cometary H_2O (Mumma et al. 1986; Weaver et al. 1986; Larson et al. 1986), the first measurements of its ortho-para ratio (and nuclear spin temperature) (Mumma et al. 1986; 1987), and the first quantitative measures of primary volatiles through remote and in situ studies (Mumma et al. 1986; Weaver et al. 1986; Combes et al. 1986). Progress in these areas expanded dramatically over the ensuing 30 years as instrumental (Mumma & Charnley 2011) and mission capabilities improved (Altwegg et al. 2015).

Nowadays, the relationship of cometary properties to origins still presents unanswered questions. For example, according to the *Nice* dynamical model (Morbidelli & Rickman 2015; Levison et al 2011, Morbidelli et al. 2000; Morbidelli 2005), comets formed in two regions of the proto-planetary disk: between $R_H \sim 5$ and 15 au and beyond ~20 au. Differences in those formative regions, such as different UV irradiation, cosmic ray bombardment, different molecular abundances, temperature and chemical pathways, should be imprinted in the icy material. If cometary nuclei were subsequently dispersed, due to dynamical instabilities among the giant planets (populating both the Oort Cloud and the Kuiper Belt reservoirs but perhaps in different proportions), can we expect comets in the different dynamical families (e.g., Jupiter Family Comets (JFCs), Long Period Comets (LPCs), Halley Type Comets (HTCs), Dynamically New Comets (DNs)) to show distinct evidence of cosmogonic differences?

Since 1996, the advent of powerful high-resolution infrared spectrometers increased the sensitivity on cometary retrievals, and that revolution continues today. Here, we present results obtained for the bright Oort cloud comet C/2017 E4 (Lovejoy) using iSHELL – the new high-resolution infrared spectrograph at NASA/IRTF. The very wide spectral range covered by iSHELL, its high

spectral resolving power, and the very high accuracy of our advanced analytical methods, eliminate many sources of systematic uncertainty that might otherwise occur when retrieving the desired cosmogonic parameter.

2. Observations and Data reduction

2.1 Observations

Comet C/2017 E4 (Lovejoy), hereafter E4 (Lovejoy), was discovered on March 9th 2017 by Terry Lovejoy (Queensland, Australia) when the comet was at ~1 au from the Sun and it had a magnitude M_v ~15. This comet reached perihelion on 23rd April 2017 at 0.49 au and its closest approach to Earth was on 30th March at 0.508 au. It disrupted completely in late April 2017 (S. Yoshida, http://www.aerith.net/comet/catalog/2017E4/2017E4.html). The JPL Horizon ephemeris (solution #11) provides values for semi-major axis (a), eccentricity (e), inclination (i) and aphelion distance (954.8 au), from which we derive the orbital period (about 10440 yr). These parameters suggest a possible origin of this LP comet from the inner Oort Cloud.

The estimated and observed rapid increase of magnitude and activity, (S. Yoshida, www.aerith.net; E. Jehin, private communications) triggered our interest in comet E4 (Lovejoy) and, during our observing campaign on comets C/2015 V2 (Johnson) and C/2015 ER61 (PanSTARRS), we observed comet Lovejoy with iSHELL at NASA/IRTF (Maunakea, Hawaii) through an approved addition of target. We acquired spectra on UT 4 April 2017 when the comet was at a heliocentric distance of about 0.66 au and at a geocentric distance of about 0.64 au on the 4th of April 2017, before its perihelion passage and several weeks prior to its complete disruption. When observed, the comet had a geocentric velocity of about 20.4 km/s, sufficient to shift the cometary emission lines from their telluric counterparts (maximizing sensitivity), and it had an infrared figure-of-merit of about 0.9 [$FoM = Q(H_2O)_{Rh} \times 10^{-29} \times R_h^{-1.5} \Delta^{-1}$] when observed. In Figure 1, we present two different perspectives of the comet's orbit and the view from Earth together with our observing setup, and we list a summary of the observing log in Table 1. Spectra were acquired in individual A and B exposures following a nodded ABBA sequence.

We observed comet E4 (Lovejoy) for about 2.5 hours with iSHELL, the new long slit near-infrared high-resolution immersion echelle spectrograph, a few months after its commissioning. iSHELL covers the wavelength range of (1.1 – 5.3) μm with a resolving power of about $\lambda/\Delta\lambda = 70,000$ when using a slit width of 0.375 arc-seconds (3 pixels wide, considering the 0.125 arc-seconds/pixel plate scale). The instrument offers 6 different cross-dispersing gratings that allow the observer to select specific wavelength ranges within the full range. The 19 available settings are selected at different tilts of the 6 cross-dispersers (Rayner et al. 2012).

We used four different iSHELL settings (Fig. 2): Setting L1-c (customized at upper wavelength 3.11 μm and covering 2.81 – 3.11μm), setting L3 (covering 3.20 – 3.48 μm), setting Lp1-c (customized at upper wavelength 3.71 μm and covering 3.33 – 3. 71 μm), and setting M1 (covering 4.52 – 5.25 μm). For our observations, we used a slit width of about 0.75 arc-seconds that corresponded to a resolving power of about $\lambda/\Delta\lambda = 35,000$. In our cometary spectra, the widths (FWHM) of the detected emission lines are best fitted with slightly higher resolving power (about $\lambda/\Delta\lambda = 55,000$), that is consistent with the general seeing conditions during the observing run. We detected nine primary volatile species (H_2O, HCN, NH_3, CO, C_2H_2, C_2H_6, CH_4, CH_3OH, H_2CO) and three product species (CN, NH_2, OH) in the spectra extracted from these four iSHELL settings.

Table 1 - Observing log on UT 4th April 2017

UT time [hh:mm]	Object	Setting	t_s^a [min]	t_{exp}^b [s], n_{coadd}	airmass	R_h [au]	Δ [au]	$d\Delta/dt$ [km/s]
13:44-13:48	BS7924	L1-c		10, 1	1.98-1.94			
13:52-13:54		L3		10, 1	1.90-1.89			
13:57-13:59		M1		10, 1	1.86-1.85			
14:03-14:05		Lp1-c		10, 1	1.81-1.79			
15:25-17:10	C/2017 E4	Lp1-c	68	60, 1	2.08-1.24	0.6637-0.6627	0.6349-0.6357	19.63 - 20.02
17:55-18:54		M1	40	15, 4	1.11-1.03	0.6622-0.6616	0.6361-0.6365	20.21 - 20.46
18:55-19:20		L1-c	20	60, 1	1.02-1.00	0.6616-0.6614	0.6365-0.6367	20.46 - 20.57
20:39-21:22		L3	28	60, 1	1.02-1.08	0.6605-0.6600	0.6374-0.6378	20.92 – 21.11

a Time on source.
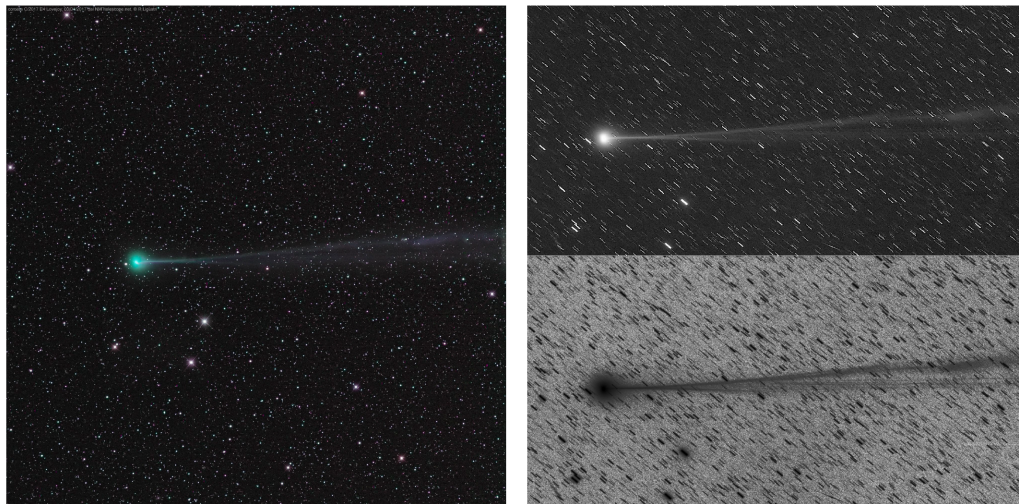b Exposure time and number of co-added frames per individual A or B exposures.
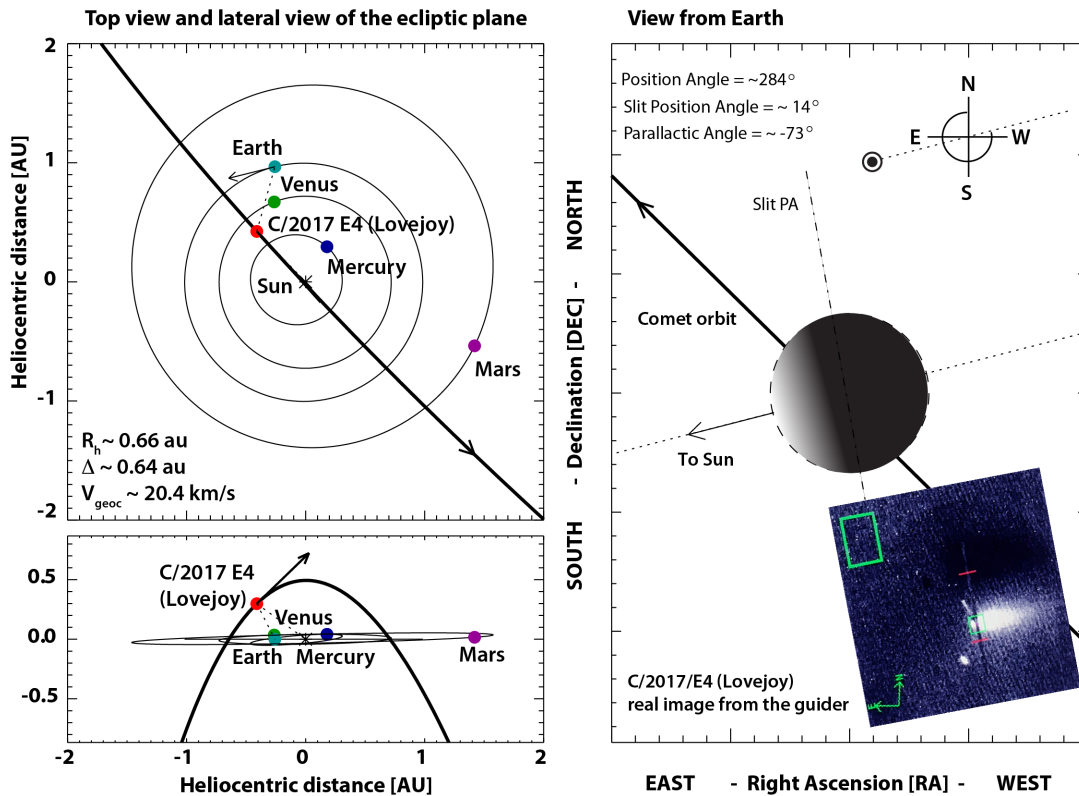
Figure 1. The orbit and aspect of comet C/2017 E4 (Lovejoy) on UT 4 April 2017.

Top and bottom left graphics show the top view and lateral view of the ecliptic plane and the orbit of comet C/2017 E4 (Lovejoy) during the observations on 4th April 2017 when the comet was at a heliocentric distance of about $R_h \sim 0.67$ au, a geocentric distance of about $\Delta \sim 0.64$ au and a geocentric velocity of about 20.4 km/s.

Right graphic shows the projected view from Earth during the observations. The comet was observed before perihelion and due to its elongated shape, we oriented the slit perpendicular to the Sun-comet direction. In the inset, a real image of the observation setup is shown; the slit appears as a dark line perpendicular to the extended coma-tail direction. The real image from the guider has been rotated for graphical purposes, in order to compare the observed coma-tail direction with the expected one. Bottom pictures credit: Rolando Ligustri NM telescope, apo 106/530 ccd PL1102 (Udine, Italy)
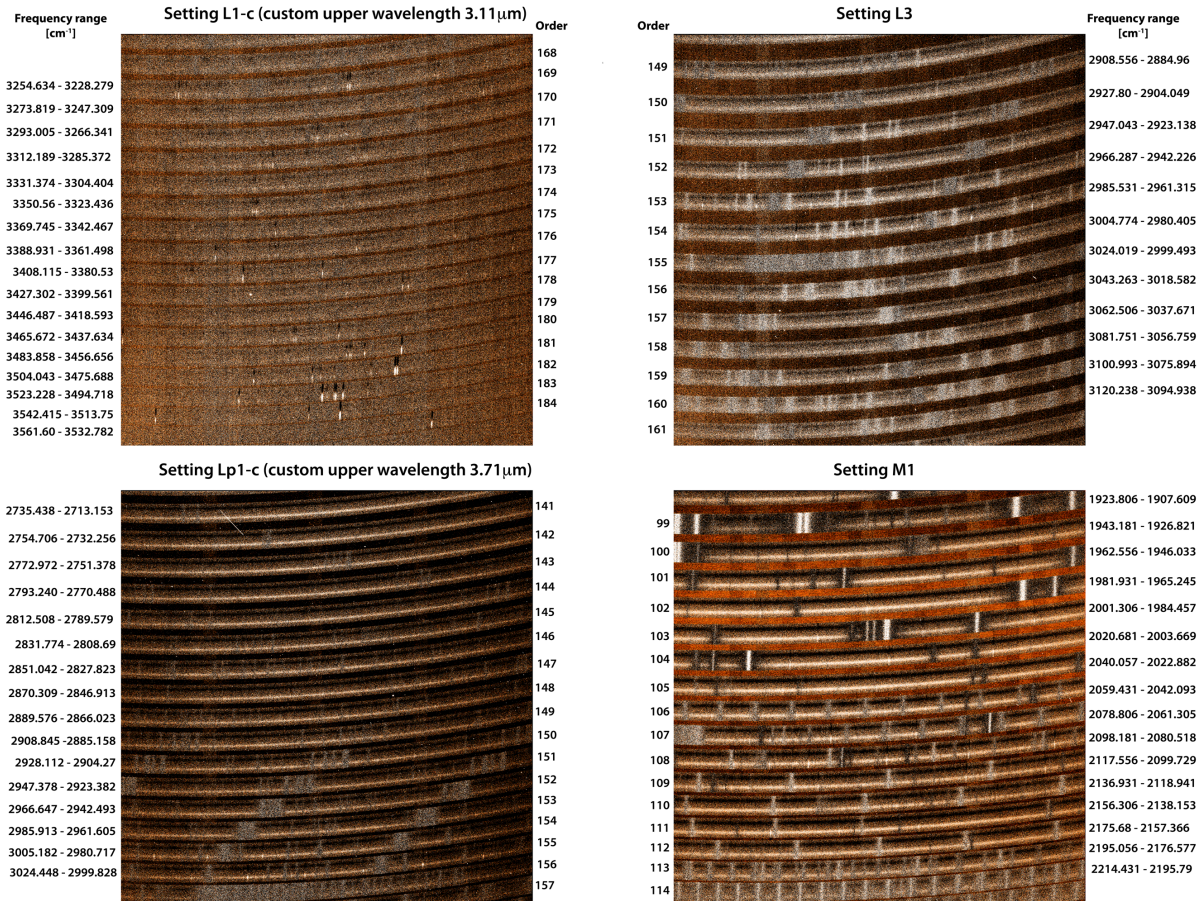
Figure 2.
iSHELL echellograms of comet E4 Lovejoy acquired on UT 4 April 2017. Each echellogram represents a stack of frames taken in ABBA nod sequences (see text). The four panels show echellograms taken with instrument settings L1-c, L3, Lp1-c, and M1. The frequency range (cm⁻¹, x-axis) and order number (y-axis) are labeled for each order. The order number increases from top to bottom for each setting. Frequency decreases (wavelength increases) from left to right within each order, and decreases (increases) from bottom to top across the echellograms. Telluric features appear throughout the echellograms along with emission from dust and gas in comet E4.

2.2 Data reduction

The raw data were processed (cleaned, straightened, and wavelength- and flux-calibrated) using the latest version of the Goddard custom algorithms for data reduction and analysis (Villanueva et al. 2013a), developed for previous spectrographs (e.g. NIRSPEC, CRIRES, CSHELL) and now tailored for iSHELL. Each cropped order in the four echellograms was processed separately - including removal of bad pixels, re-sampling in wavenumber, and straightening of optical curvature. In support of the data reduction, we also developed an echelle simulator for iSHELL (Faggi, Villanueva and Mumma 2017: https://psg.gsfc.nasa.gov/apps/ishell.php). It employs a set

of ab-initio grating equations and uses simplified parameters that are accurate enough to describe the overall behavior of the cross-dispersers and the gratings.

The frequency calibration was performed by fitting the terrestrial radiance spectrum with PSG, the Planetary Spectrum Generator (https://psg.gsfc.nasa.gov (Villanueva et al. 2018)). In synthesizing the telluric radiance spectrum, we retrieved the vertical profile of temperature and trace gases atop Maunakea using the extremely accurate NASA/MERRA-2 atmospheric and climatological repository (Gelaro et al. 2017) (https://gmao.gsfc.nasa.gov/reanalysis/MERRA-2/) accessed through the PSG tool. The powerful combination of PSG with NASA/MERRA-2 permits reproduction of realistic atmospheric conditions and abundances for any site on Earth, with a precision of 30 minutes in the temporal interval from 1981 until now. The vertical profiles are evaluated from Earth's surface up to 70 km with a spatial resolution of about 1 km.

The cometary data were flux-calibrated order-by-order relative to the standard star flux (BS 7924) using the conversion efficiency (gamma, Γ_v) derived from the top-of-atmosphere stellar flux density [W /m^2/cm^{-1}], the modelled atmospheric transmittance, and the measured instrumental counts per pixel [ADU/s]. Extracted values for mean gamma of individual orders are given in Table A.1 of Appendix (complete list is presented as online material).

3. Data Analysis

3.1 Rotational temperature and nuclear production rates of primary species

The rotational temperature (T_{rot}) is the temperature that defines the population distribution among rotational levels in the ground vibrational state of a given molecule. Neutral–neutral collisions with H_2O thermalize trace gases in the near-nucleus coma, while electron collisions thermalize the ground ro-vibrational states of H_2O and other neutral species in the intermediate coma (Xie and Mumma 1993). Accurate evaluations of T_{rot} are the key to extracting reliable production rates. Rotational temperatures and nucleus-centered production rates in comet E4 (Lovejoy) were retrieved for spectra extracted from 15 pixels along the slit, centered on the nucleus position and spanning about ± 1.252 arcsec from the nucleus itself in the setting L1-c (i.e. ± 546.34 km considering a plate scale of about 0.167 arcsec/pix); ± 1.403 arcsec (i.e. ± 611.75 km considering a plate scale of about 0.187 arcsec/pix) in L3; ± 1.245 arcsec from the nucleus in the setting Lp1-c (i.e. ± 543.07 km considering a plate scale of about 0.166 arcsec/pix); and ± 1.238 arcsec (i.e. ± 539.80 km considering a plate scale of about 0.165 arcsec/pix) for setting M1. (these plate scales are adopted from the iSHELL User's Manual - version July 2017).

We applied two different approaches for rotational analysis: the correlation- and excitation-methodologies developed by the Goddard team (Bonev 2005; Villanueva et al. 2008). The correlation method is based on the evaluation of the correlation coefficient between the observed and the synthetic spectrum, identifying the temperature that produces the best correlation (see Fig 3, panel b). The second method, slope analysis method, evaluates the rotational temperature considering the relation between the observed and the predicted flux ratio, and the mean value of pumping rotational state energies in the ground vibrational state (see Fig 3, panel a, c, d, e, f). Because the line fluxes are related to the populations of rotational levels in the upper vibrational state E_{up} and reflect the temperature dependent distribution of the ground state (000), measurements of individual emission lines that span a wide range of ground-state excitation energies (along with state-of-the-art line-by-line emission models with full fluorescence cascade) are recommended to provide accurate retrievals.

Rotational temperatures were evaluated for H_2O, HCN, NH_3, CO, C_2H_2, C_2H_6, CH_4, CH_3OH, and H_2CO. Nucleus-centered production rates were retrieved from each ro-vibrational detected line, comparing the calibrated fluxes (corrected for the terrestrial transmittance at the Doppler-shifted line frequencies) with the fluorescence efficiencies (g-factors [photons/molecules/s]) obtained at

specific T_{rot} [K], as derived from the quantum mechanical fluorescence models developed by the Goddard team (Villanueva et al. 2012a; 2012b; DiSanti et al. 2006; Villanueva et al. 2011a; 2013b). The ratio of measured and modelled line intensity for each line was graphed against mean excitation energy for the specific value of T_{rot}, and the slope was determined. The specific value of T_{rot} was varied until the slope of the fitted lines was zero. All the applied fluorescence models considered realistic solar pumping fluxes generated by the combination of the empirical high-resolution line-by-line solar emittance spectrum (Hase et al. 2006) combined with a theoretical solar model for continuum irradiance (Villanueva et al. 2011a). In retrieving nucleus-centered production rates, we took into account the fraction of total molecules contained in the beam under the assumption of spherically symmetric outflow at uniform velocity. The values obtained for rotational temperatures and nucleus-centered production rates are reported in Table 2, third and fourth columns.

Examples of excitation analyses are shown in Figure 3. In panel a, c, d, e, f, the slope analysis method is reported. The x-axis represents the ground-state rotational energy [cm^{-1}] of the principal pumping transitions and the y-axis represents the molecular production rate [Q(H$_2$O), units of 10^{29} s^{-1}, Q(HCN), Q(CH$_4$), Q(C$_2$H$_6$), units of 10^{25} s^{-1} , Q(CO), units of 10^{26} s^{-1}] extracted from any individual line. In panel a, Ortho- and para-water lines for L1-c and M1 setting are shown in two different shades of blue and green respectively. The graphic shows the line-by-line values of water production rate returned at the optimum rotational temperature (T_{rot}= 78 K), which corresponds to the linear fit with slope equal to zero (dotted line). Panel b shows the comparison of water rotational temperature derived from the slope analysis method (dark blue) and from the correlation analysis method (light blue). The x-axis represents the rotational temperature T_{rot} [K]. The left y-axis reports the scale for the correlation coefficient while the right y-axis reports the scale for absolute values of slope [in units of 10^{-5}].

Table 2. Parameters for Primary Volatiles Detected in C/2017 E4 (Lovejoy).

Primary Volatile	Setting	T_{rot} [K][a]	Q_{nc} [s^{-1}] x10^{25}	Q_{scale}	Q_{tot}[b] [s^{-1}] x10^{25}	Mixing ratio w.r.t. H$_2$O[d] [%]
H$_2$O[c]	L1	81±3	1686.3 ± 47.3	1.84 ±0.04	3164.69 ± 108.01	100
	M1	75±11	2037.4 ± 61.8	1.78 ±0.16		
	L1 + M1	78±3	1685.6 ± 39.5			
CH$_3$OH	Lp1	83±5	31.47 ± 1.00	1.63 ±0.07	51.14 ± 2.53	1.62 ± 0.10
	L3	(78)	27.52 ± 3.43	1.87 ±0.15		
HCN	L1	(78)	2.86 ± 0.24	1.84 ±0.04	5.29 ± 0.45	0.17 ± 0.02
NH$_3$	L1	(78)	31.88 ± 6.06	1.84 ±0.04	58.93 ± 11.29	1.86 ± 0.36
H$_2$CO	Lp1	84±10	6.92 ± 0.44	1.63 ±0.07	11.25 ± 0.87	0.36 ± 0.03
C$_2$H$_2$	L1	(78)	2.34± 0.31	1.84 ±0.04	4.32 ± 0.57	0.14 ± 0.02

C_2H_6	**Lp1**	**81±10**	**8.33 ± 0.27**	*1.63 ± 0.07*	**12.25 ± 0.60**	**0.39 ± 0.02**
	L3	**(78)**	**5.21 ± 0.41**	*1.63 ± 0.07*		
CH_4	**L3**	**(78)**	**5.84 ± 0.53**	*1.63 ± 0.07*	**10.91 ± 1.33**	**0.34 ± 0.04**
CO	**M1**	**(78)**	**20.57 ± 1.71**	*1.78 ± 0.16*	**36.64 ± 4.56**	**1.16 ± 0.15**

[a] When a rotational temperature was obtained using the excitation analysis method, the derived confidence limits (± 1-σ) are shown. Values for T_{rot} in parenthesis, without confidence limits, are adopted from the weighted mean of measured values of T_{rot} for H_2O.

[b] Total production rates were obtained from nucleus-centered values, after slit-loss correction (Q_{scale}) for each setting. For water, methanol and ethane we report the weighted average values using independent slit-loss corrections. For the molecules emitting in setting Lp1 and L3, we adopt the Q_{scale} factors derived from the brightest lines of C_2H_6 present in the two settings respectively. In setting L1-c, we adopted the Q_{scale} factor for co-measured lines of H_2O and HCN to correct the slit-losses for the species present in that setting. The Q_{scale} factor in M1 was retrieved from the brightest lines of CO and water.

[c] Water rotational temperatures and nucleus-centered production rates have been measured both for L1 and M1 settings separately (first two rows) and simultaneously (third row). Growth factor corrections have been applied for the independent retrievals in settings L1 and M1, respectively. The total production rate is then evaluated as the weighted mean of such single global production values.

[d] Mixing ratios relative to water are reported. The confidence limits reflect the weighted accuracy of production rates retrieved independently in different settings.

Examples of fully analyzed cometary spectra are given in Fig 4. The extracted spectra from order 171 and 182 of setting L1-c, from order 147 and 155 of Lp1-c setting, from order 157 of L3 and from order 109 of M1 are shown in black in the top part of the six plots. The continuum synthetized with PSG, affected by terrestrial atmospheric transmittance, is superimposed in grey (superposed and below). Examples of cometary molecular residuals (after continuum subtraction) and of the modeled spectra for fluorescent emission from detected molecules (NH_3, HCN, C_2H_2, NH_2, H_2O, CN, CO), are reported in the middle traces of the graphic (using different colors), and superimposed (all molecules, red). The lower-most trace shows the spectral residuals after subtracting the modeled molecular detections; the ±1-sigma error level is displayed in green. The observed fluxes [Wm^{-2}/cm^{-1}] are shown with respect to frequency [cm^{-1}] and wavelength [μm]. The scale of the x- axis is shown in frequency [cm^{-1}] below each panel and shown in wavelength [μm] above each panel. In the two top panels, molecular emissions from H_2O, HCN, NH_3, NH_2, and C_2H_2 in order 171 (L1-c) and in order 109 (M1) from H_2O, CO, and CN (the 1-0 fundamental vibrational band of the $X^1\Sigma^+$ system) are shown. In the middle panels, we report emissions from CH_3OH, H_2CO and OH, and from CH_3OH and C_2H_6, in orders 147 and 155 (Lp1-c) respectively. In the bottom panels, simultaneous detection of the two nuclear spin isomers (ortho- and para-water) in order 182 (L1-c); and detections of CH_4 and NH_2 in order 157 (L3) are presented. Examples of detailed description of individual molecular emission lines is reported in the Table A2 in the Appendix (the complete list of the detailed description of individual line for all the detected molecules is provided as online material).
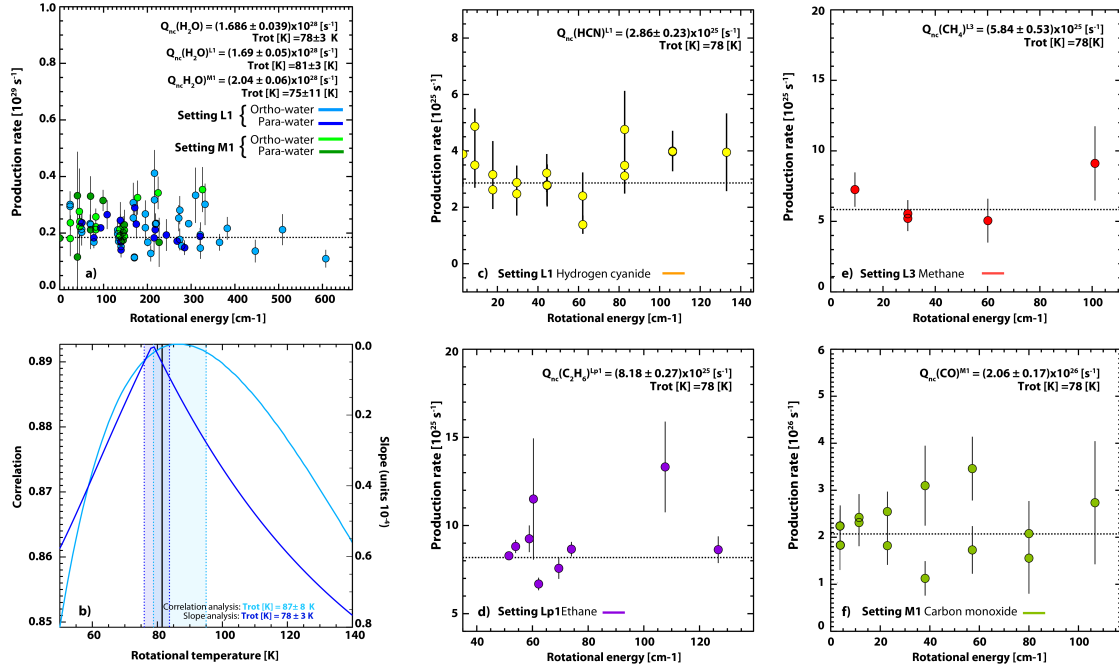
Figure 3 Excitation analyses in comet C/2017 E4 Lovejoy.
Panel a, c, d, e, f shows the excitation analysis for water (in setting L1-c and M1), hydrogen cyanide (setting L1-c), methane (setting L3), ethane (setting Lp1-c) and carbon monoxide (setting M1). Panel b: Comparison of the rotational temperature derived from the slope analysis method (dark blue) and from the correlation analysis method (light blue).
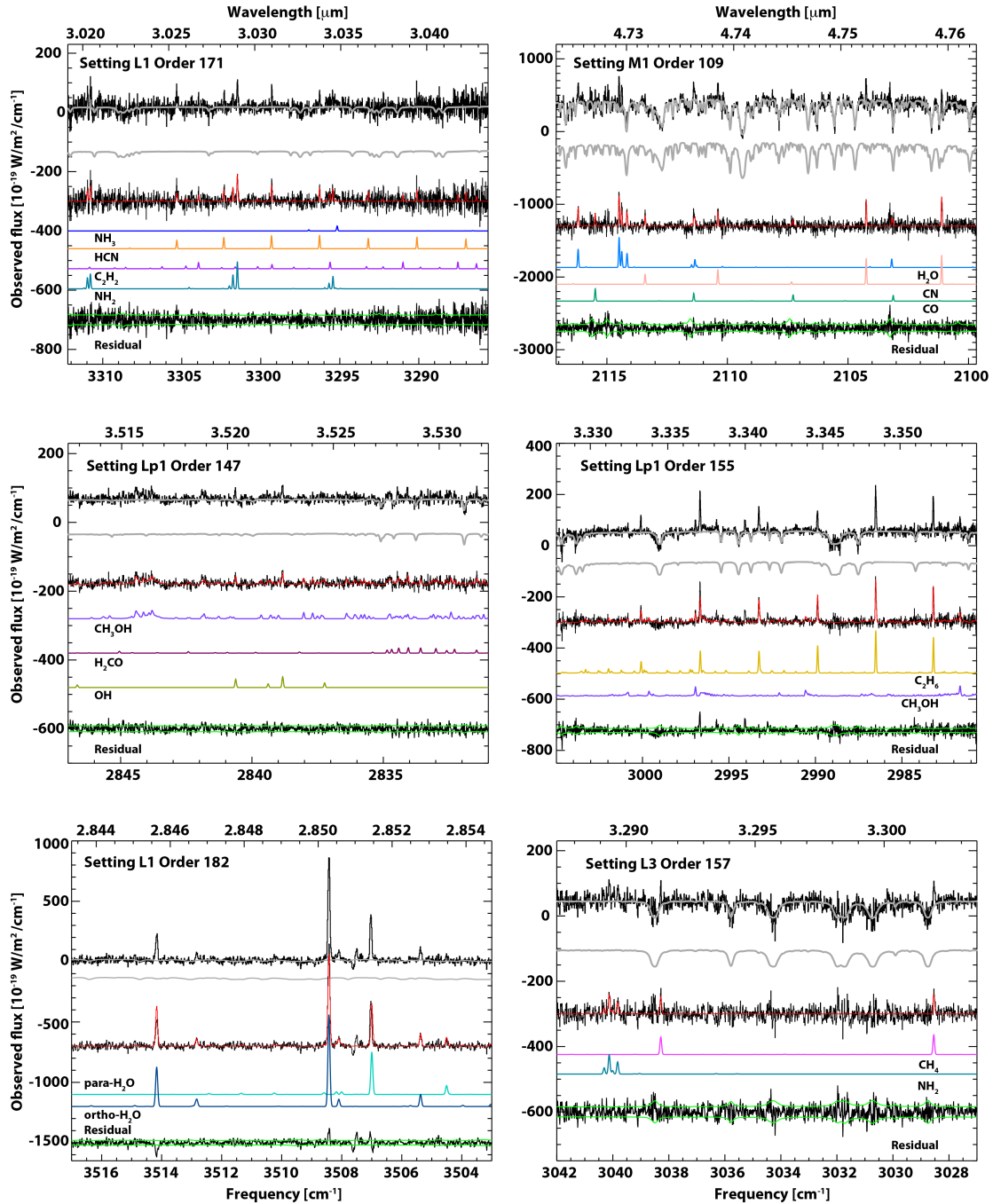
Figure 4
Each panel shows cometary spectra extracted from a specific order of the four iSHELL echellograms. Cometary spectra are shown and compared with optimized synthetic spectra for detected species. See discussion §3.1. The modelled emission spectra are shown shifted downward along the y-axis relative to the residual cometary spectrum, for clarity. The lowest trace in each panel is the grand residual after subtracting the modelled emissions from the measured molecular residual; the expected stochastic noise envelope (± σ) is shown in green.

3.2 Spatial profiles and total production rate

To properly correct for 'slit-losses' introduced by atmospheric seeing we performed a detailed analysis of the spatial profiles for the brightest observed lines in the coma. The turbulence of Earth's atmosphere produces a spread of the flux from a point source causing signal reduction in the central part of the object; the resulting image degradation is a measure of the 'seeing'. An object-centered aperture that is smaller than the telescope's point-spread-function (PSF) will measure a reduced flux from the object. The measured signal will be smaller in the nucleus-centered region than it would be without 'seeing'. For an extended source such as a comet, the needed correction decreases rapidly with increasing nucleocentric distance owing to the successively slower decrease in surface brightness in the coma.

Long-slit spectroscopy permits compensation for 'slit losses' by performing the "Q-curve methodology" correction (Xie et al. 1996; Dello Russo et al. 1998). This methodology is based on the analysis of spatial profiles for the selected molecular species through the evaluation of production rates at well-defined intervals along the slit. Under the hypothesis of spherically symmetric outflow at uniform velocity (Mumma et al. 2003), we computed the '*spherical production rates*', i. e. the production rates extracted at different spatial intervals from the nucleus-centered region: $Q_i = Q_1, Q_2, Q_3, \ldots Q_n$; where each value was obtained taking the weighted mean of the up- and down-value at symmetric spatial distance from the nucleus position (i.e. $<Q_i> = 0.5*(Q_{i+} + Q_{i-})$, see Fig 5. This series in (Q_i) is termed a "Q-curve", and the region where Q_i reaches a plateau is called the "terminal region" and the weighted mean Q_i in this region is called the "*terminal production rate (Q_{term})*". In order to evaluate the global production rate, we retrieve a correction factor, called the "*growth factor (Q_{scale})*", namely, the ratio between the terminal production rate and the nucleus-centered production rate (growth factor $Q_{scale} = Q_{term}/ Q_{nc}$). The slit loss correction is then performed by multiplying the nucleus-centered production rates by the growth factor ($Q_{tot} = Q_{scale} \times Q_{nc}$), see Table 2. This methodology is well documented in the literature; (e.g., DiSanti et al. 2014; Villanueva et al. 2011b).

For comet E4 (Lovejoy), we selected intervals of 5 pixels along the slit and we defined boxes of 25 pixels (5 pixels in the spatial direction × 5 pixels in the spectral direction) from which we evaluated the spherical production rates, Q_i. The nucleus-centered production rate (Q_{nc}), as already mentioned in Section 3, was obtained from the production rates Q_{-1}, Q_0, Q_1, sampling 15 pixels

along the slit (three boxes of 25 pixels), centered on the nucleus position. The nucleus-centered production rate (Q_{nc}) does not correspond to the sole Q_0, which represents the production rate extracted from 5 pixels in the center position. Instead Q_{nc} corresponds to the combination of Q_{-1}, Q_0, Q_1 because it represents the maximum signal-to-noise ratio in the extracted spectra. The terminal production rates (Q_{term}) were obtained as the weighted mean of the production rates Q_{-3}, Q_{-2}, Q_{-1}, Q_1, Q_2, Q_3, extracted at intervals of 5 pixels stepped along the slit, starting at ± 2 pixels from the central position, and spanning 15 pixels upward and downward along the slit (see Figure 5).

In deriving the growth factor (Q_{scale}), we analyzed the spatial profiles of the brightest lines of H_2O in L1-c and M1 settings, of C_2H_6 in L3 and Lp1-c settings, of HCN in L1-c setting, and CO in M1 setting. We retrieved 4 distinct growth factors, one for each setting, as the weighted mean of the growth factors evaluated on the mentioned brightest molecular line for each setting. The values are reported in Table 2 along with the computed total molecular production rate for each species. In Figure 5 we show the spatial profile analysis. In the panel a, the spatial profiles of molecular outgassing of water in setting L1-c and ethane in setting Lp1-c are reported along with the dust morphology profiles evaluated from the spatial profiles of the continuum in the same settings. The continuum profile per each setting, reported in the plot, is computed as the weighted mean of the continuum spatial profiles extracted for each order of a specific setting. In the panel b, we compare more noisy spatial profiles of water and CO acquired in M1, HCN from L1-c, and ethane from L3, together with the spatial profile for the continuum in their respective settings. Both panels show the PSF extracted from the calibration standard star.

The outgassing of such species in comet E4 (Lovejoy) showed particularly symmetric profiles along the slit. This is consistent with the slit being oriented orthogonal to the cometary-Sun position angle direction (see Section 2, Figure 1) and also with the morphology revealed by the coma image taken during the observing (Figure 1, right).

The column densities for gases and dust in comet E4 (Lovejoy) showed particularly symmetric profiles along the slit. This is consistent with either uniform spherical outflow or with axial outflow symmetric about the sun-comet position, either case being consistent with the growth factor formalism and global Q's presented here (Xie and Mumma 1996). The slit was oriented orthogonal to the comet-Sun position angle direction (see §2, Figure 1) and also with the coma image taken during the observing (Figure 1, right).
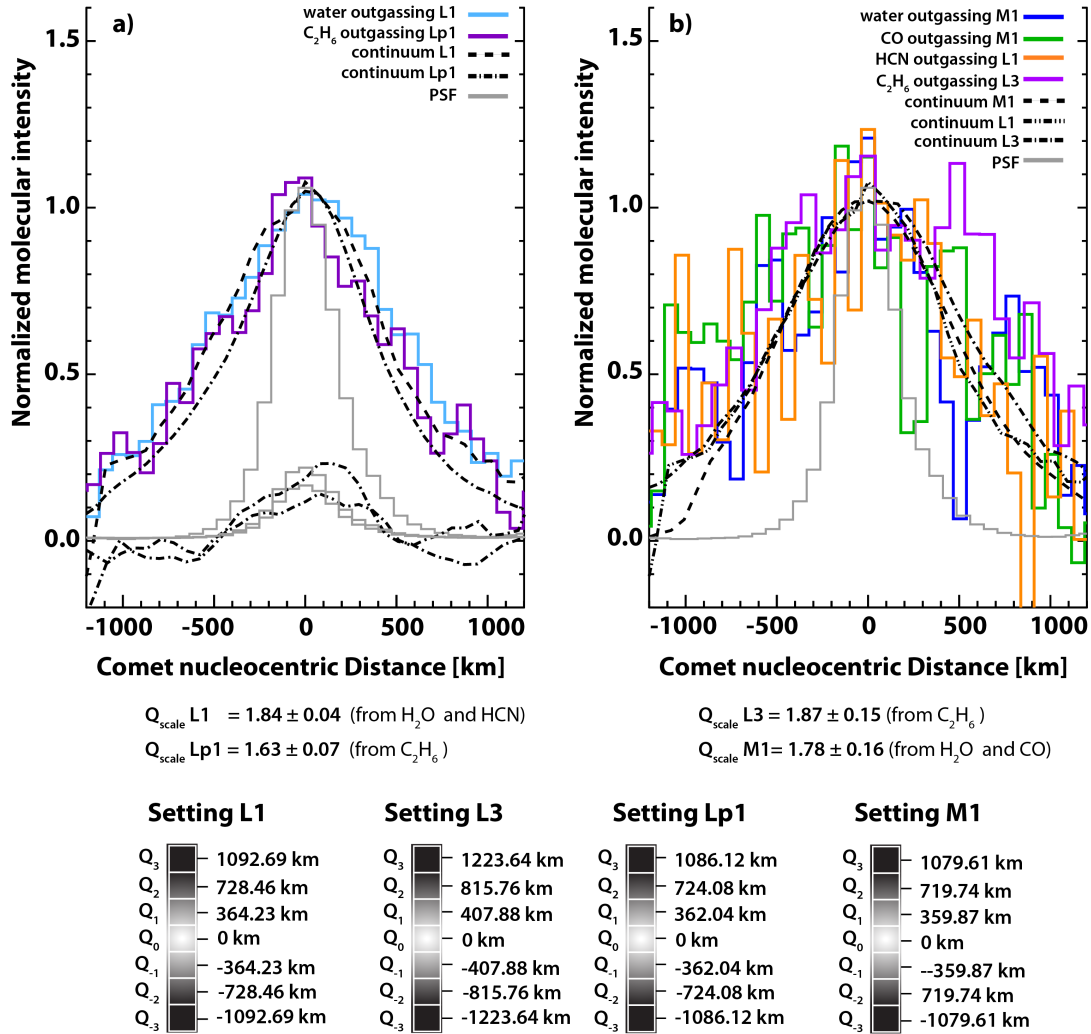
a)

Legend (panel a):
- water outgassing L1
- C_2H_6 outgassing Lp1
- continuum L1
- continuum Lp1
- PSF

b)

Legend (panel b):
- water outgassing M1
- CO outgassing M1
- HCN outgassing L1
- C_2H_6 outgassing L3
- continuum M1
- continuum L1
- continuum L3
- PSF

Q_{scale} L1 = 1.84 ± 0.04 (from H_2O and HCN)

Q_{scale} Lp1 = 1.63 ± 0.07 (from C_2H_6)

Q_{scale} L3 = 1.87 ± 0.15 (from C_2H_6)

Q_{scale} M1 = 1.78 ± 0.16 (from H_2O and CO)

Setting L1

Q_3	1092.69 km
Q_2	728.46 km
Q_1	364.23 km
Q_0	0 km
Q_{-1}	-364.23 km
Q_{-2}	-728.46 km
Q_{-3}	-1092.69 km

Setting L3

Q_3	1223.64 km
Q_2	815.76 km
Q_1	407.88 km
Q_0	0 km
Q_{-1}	-407.88 km
Q_{-2}	-815.76 km
Q_{-3}	-1223.64 km

Setting Lp1

Q_3	1086.12 km
Q_2	724.08 km
Q_1	362.04 km
Q_0	0 km
Q_{-1}	-362.04 km
Q_{-2}	-724.08 km
Q_{-3}	-1086.12 km

Setting M1

Q_3	1079.61 km
Q_2	719.74 km
Q_1	359.87 km
Q_0	0 km
Q_{-1}	-359.87 km
Q_{-2}	719.74 km
Q_{-3}	-1079.61 km

Figure 5. Spatial profiles measured for multiple molecular volatiles in comet C/2017 E4 Lovejoy.
The normalized molecular intensity in relative units is reported on the y-axis with respect to the nucleus-centered distance [km], x-axis. Below the panels, the four values of Q_{scale} evaluated for each setting are reported.
On the bottom part of the figure we report the spatial boxes that define the integration area in which we computed the nucleus-centered and the terminal production rates and from which we evaluated the growth factor for each setting are shown. The spatial box (Q_0) is located at the center of the slit and it spans 5x5 pixels. Upper and lower spatial boxes are labeled as Q_{-n} and Q_n respectively. Nucleus-centered production rates are extracted from Q_{-1}, Q_0, Q_1, while spherical production rates are evaluated for Q_{-3}, Q_{-2}, Q_{-1}, Q_1, Q_2, and Q_3. An example of object centered in the box (Q_0), located at the center of the slit, is reported just for explanatory graphical purposes. Left and right panels distinguish between less noisy and more noisy profiles. In the panel a, water in setting L1-c and ethane in setting Lp1-c are shown and compared to the cometary continuum profile (different dashed black lines) of each setting, and the star profile (solid gray line). In the lower part of the plot a residual nuclear component is shown and compared with the 15%-20% of the PSF. This component is obtained as the difference between the continuum and the gas emission profiles for water in L1 and ethane in Lp1 (scaled to a common profile in the wings). In the panel b, we show the spatial profiles of water and CO in M1, HCN in L1-c, and ethane in L3. Such profiles are compared to the cometary continuum profile (different dashed black lines) of each setting respectively, and to the star profile (solid gray line). A residual nuclear component cannot be obtained because of the noisy profiles.

16

4. Results and Discussion

4.1 Water production rate, Ortho-to-Para Ratio and Spin Temperature

We detected 85 water lines from 12 different vibrational bands across L1-c and M1 settings (Fig. 6). In setting L1-c in the (2.8 – 3.0) μm range of setting L1-c, we detected 58 water lines from 8 vibrational water bands, six of which represent non-resonance fluorescence (201-200), (101-001), (200-001), (200-100), (101-100), and (111-110), and two are resonance fluorescence bands (100-000) and (001 – 000). In the (4.5 – 5.1) μm range of setting M1, we detected 27 water lines from 4 vibrational water bands; all are in non-resonance fluorescence (100 - 010), (101 - 110), (001-010), and (011-020).

In Figure 6 the observed frequencies [cm^{-1}] and flux intensities [ADU] of individual water lines (in black) from setting L1-c and M1 are compared with predictions of the Goddard water fluorescence model (in red) (Villanueva et al. 2012b); a quantitative description of the detected lines is reported in Table A2. Water rotational temperatures and production rates were retrieved both separately and simultaneously for L1-c and M1 settings, using the two excitation analysis methods (slope and correlation analysis methods, see section 2). From the slope analysis method (Figure 3, panel 'a'), the rotational temperature obtained from the simultaneous retrieval (L1-c and M1 combined) is (78 ± 3) K, while the values obtained from the individual settings are (81 ± 3) K for L1-c and (75 ± 11) K for M1. The values of T_{rot} for individual settings are consistent with each other and also with the combined (L1-c and M1) analysis.

The confidence limits for T_{rot} were computed from the statistical errors of the slope analysis that were selected considering the higher of the stochastic error (the uncertainty of individual values produced by photon noise) and the variance error (standard error), that describes the spread of the derived quantities around the slope line. We obtained a stochastic error for the slope zero that corresponds to an interval of about ± 3 K in temperature for the simultaneous retrieval, as shown in Fig. 3, panel b.

In the same chart, the temperature-correlogram plot is shown (Correlogram Factor vs. T_{rot}, in blue) for comparison. From the correlation analysis, the retrieved rotational temperature is about ~ 87 K at the maximum correlation of about 0.89. The sharper the correlation curve is, the more accurate the retrieval of T_{rot}. For the correlation analysis, the adopted confidence limits are about ± 8 K. We selected the greater value between the slope analysis method and a chi-square minimization

process, based on Levenberg-Marquardt non-linear minimization fitting (Villanueva et al. 2011b), in which all the molecular detected species are fitted simultaneously order-by-order.
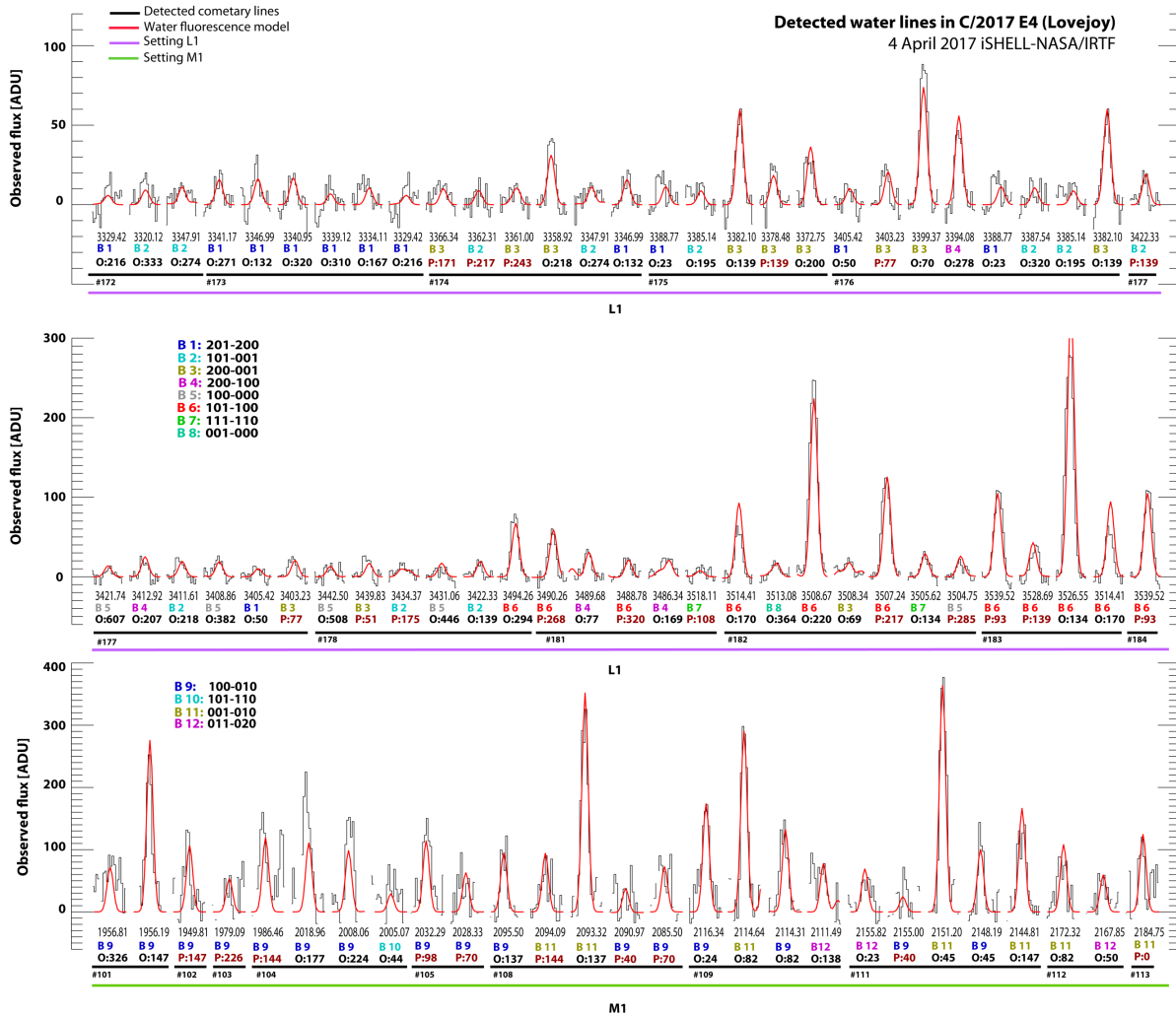

Figure 6. Spectral lines of H₂O detected in E4 Lovejoy. The 85 identified water lines in the ~ 3 μm and ~5 μm regions span over 21 spectral orders of L1-c and M1 iSHELL echellograms. The y-axis reports the observed line intensities [ADU], while the setting (purple and green bars) and the order ranges (horizontal black bars) are reported on the x-axis, along with the (rest) wavenumber [cm⁻¹], vibrational band (B1-B12, see legend), nuclear spin isomer (O for ortho, P for para) and mean state rotational energy level [cm⁻¹] for each line. The observed positions and intensities of individual lines (black) are compared with predictions of the water fluorescence model (red).

We use this method to provide a complementary process to retrieve molecular abundances and rotational temperatures and to obtain highly accurate molecular residuals on which we perform the excitation analysis methods.

The retrieved rotational temperatures and production rates obtained with the slope analysis method and the chi-square technique are practically the same, they are indeed strictly in agreement for all the molecules (e.g., water production rates agree at 97%, ethane production rates agree at 99%,

acetylene production rates agree at 93%, methanol production rates agree at 87%, etc.). However, the slope analysis provides more accurate quantification of retrieved parameters because it is an iterative process based on the excitation analysis (line-by-line F/g transition ratios for a given T_{rot} are compared to the mean excitation energies for that line).

We performed a detailed analysis of the two spin isomeric forms of water, the ortho- and the para-water. The water molecule (H_2O) has the intrinsic property to exist in two distinct forms, depending on the orientation of the nuclear spin of the two hydrogens. When the spins (S, units $h/2\pi$) are parallel the molecule is in a state (ortho) with total nuclear spin S=1, and the wave function is described by three symmetric spin states, while when the spins are anti-parallel the molecule is in a state (para) with total nuclear spin S=0, and the spin-wave function is described by one anti-symmetric spin state. Because water spin isomers don't interact radiatively under electric-dipole selection rules, spin-conversion is strictly forbidden. The lowest para-energy level and the lowest ortho-energy level differ by about 23.8 cm^{-1} (i.e. ~34 K). Thus, the Ortho-to-Para ratio, i.e., the ratio between the total populations of ortho- and para- states, depends on the temperature at which the spin state was last set, called T_{spin}. The rotational states within each spin ladder are set easily by collisions and radiation but owing to the difficulty in spin conversions the spin and rotational temperatures need not be the same.

Studies of abundance ratios of spin species detected in cometary comae, such as water, ammonia, methane, acetylene, etc., can provide valuable hints on cometary formative regions. Several species in multiple comets (H_2O, CH_4, NH_3) showed broadly consistent spin temperatures around ~30 K (Mumma & Charnley 2011), however the reliability of water-OPR as a cosmogonic thermometer is under debate. Although the common agreement around ~30 K suggests similar controlling factors, recent laboratory works suggest that the ortho-to-para ratio (OPR) in water may change under certain irradiation conditions or during surface processing (Buntkowsky et al. 2008; Sliter et al. 2011; Hama & Watanabe 2013; Hama et al. 2011). The situation is not yet clear, moreover ammonia (NH_3) and methane (CH_4) have not been characterized by laboratory experiment and the lack of a statistically significant sample of measurements in comets prevents the validation of cosmogonic significance for OPRs.

In Fig. 7 the water ortho-to-para ratio measured in 18 comets is shown along with the value retrieved in E4 (Lovejoy), which is based on simultaneous and independent water measurements for the L1 setting and M1 setting, respectively. The value retrieved for E4 is unusually accurate,

because of the large number of water lines detected with good SNR.

The retrieved OPR values are (2.49 ± 0.10) for L1-c and (2.93 ± 0.29) for M1, and are consistent with the value obtained from the two settings analyzed together (2.52 ± 0.09) which corresponds to a spin temperature of $29.42^{+1.55}_{-1.83}$ K.

Figure 7. The ortho-to-para ratio in water in comet C/2017 E4 Lovejoy.
The x-axis represents the molecular spin temperature T_{spin}[K] and the y-axis represents the water ortho-to-para ratio. The full line (black) is the theoretical ortho-to-para ratio computed as the ratio between the ortho- and the para-partition functions evaluated at specific temperatures. The water OPR for comet E4 is shown in red and it is compared with the measured values for other comets reported in literature (see color legend) (Mumma et al. 1988; 1986; Crovisier 1997; Crovisier et al. 1999; Bonev et al. 2013; Wilson et al. 2017; Dello Russo et al. 2006; 2005; Kawakita et al. 2006; 2009; Shinnaka et al. 2011; Bonev et al. 2008; Faggi et al. 2016; Paganini et al. 2012; 2015; Woodward et al. 2007; Bockelée-Morvan et al. 2009; Paganini et al. 2014a; Paganini et al. 2014). The confident limits ($\pm 1\sigma$) are shown as horizontal dashed red lines. The obtained OPR in comet E4 Lovejoy corresponds to a spin temperature (T_{spin}) of 29.4 K. In the blue box an expanded view of the measurement obtained with iSHELL is offered.

4.2 Molecular abundances relative to water

The highly favorable geocentric radial velocity (~ 20.4 km s^{-1}) provided excellent displacement of spectral lines of cometary CO and CH$_4$ from their telluric counterparts. CO emission was detected in orders 109, 110, 111, and 112 of setting M1, together with water and radical CN (whose analysis will be presented in a future paper); carbonyl sulfide (OCS) was not detected (Figure 3). Methanol and ethane were detected in Lp1-c and L3, across orders 147, 149, 154, and 155, respectively, and methane was detected across orders 157, 158, and 159 of setting Lp1-c. In setting L3, together with the afore mentioned methanol and ethane, we detected H$_2$CO in orders 143, 144, 145, and 147. Finally, setting L1 offered detections of ammonia, acetylene, hydrogen cyanide, and water across orders 168, 169, 170, 171, 172 and 173. Spectral lines of radical NH$_2$ were detected over a very wide range of wavelengths (2.9 – 3.25 µm); their analysis will be presented in a future paper. Spectral lines of radical hydroxyl were detected in prompt emission over the range 2.9-3.7µm and were used as a direct proxy for H$_2$O photolysis.

We applied the slope- and correlation-analysis methods (§3.1) to the eight trace molecular species detected across these four settings of iSHELL. In Figure 3 (panels c, d and e), we show explanatory examples of the excitation analyses for HCN, CH$_4$ and CO.

To evaluate molecular nucleus-centered production rates, we extracted rotational temperatures (T$_{rot}$) for the spectra centered on the nucleus position, as already mentioned in the previous section (§3.1 and §3.2). Accurate values of T$_{rot}$ were retrieved for H$_2$O, CH$_4$, C$_2$H$_6$, and H$_2$CO, and all were consistent with 78K (Table 2). When retrieving molecular abundances, a fixed rotational temperature of 78 K was assumed for gases whose retrieved confidence limits for T$_{rot}$ were otherwise not sufficiently accurate (>10 K) (Table 2). For example, the rotational temperatures of T$_{rot}$(HCN) = (76 $\pm$ 19) K, of T$_{rot}$(CH$_4$) = (83 $\pm$ 32) K, of T$_{rot}$(NH$_3$) = (66 $\pm$ 22) K, of T$_{rot}$(C$_2$H$_2$) = (102 $\pm$ 30) K, of T$_{rot}$(CH$_3$OH) = (98 $\pm$ 50) K in setting L3, of T$_{rot}$(C$_2$H$_6$) = (98 $\pm$ 20) K in setting L3 and of T$_{rot}$(CO) = (71 $\pm$ 13) K were assumed to be 78K. The assumed rotational temperature was verified not to alter the retrieved molecular production rates within 10%. In Table 2, a detailed collection of retrieved molecular nucleus-centered production rates is reported for all the species analyzed, along with the growth factors and slit-loss corrected production rates.

Molecular abundances relative to water are reported numerically in Table 2 and are presented in Figure 8 in a more illustrative fashion. In Figure 8, the molecular composition of comet E4 (Lovejoy) is compared with relative to reference abundance values of Oort Cloud comets extracted

as the median values from the compilation of values in the Goddard database and rescaled as unity for each species. The reference molecular abundance values are reported in the order of volatility from the least-volatile species on the left to the most-volatile species on the right: $T_{subl}(CH_3OH) \sim$ 99 K, $T_{subl}(HCN) \sim 95$ K , $T_{subl}(NH_3) \sim 78$ K , $T_{subl}(H_2CO) \sim 64$ K , $T_{subl}(C_2H_2) \sim 57$ K, $T_{subl}(C_2H_6)$ ~ 44 K , $T_{subl}(CH_4) \sim 31$ K , $T_{subl}(CO) \sim 25$ K (Yamamoto 1985; Mumma, et al. 1993). The comet E4 mixing ratios are also compared with respect to two other two disrupting comets: C/2012 S1 ISON and C/1999 S4 LINEAR, before dissolution. The three comets exhibit interesting behavior in their abundance ratios. Most molecular abundances of comet E4 (Lovejoy) are within the reference abundance ranges except for enhanced ammonia, but all three disrupting comets are generally depleted in methanol and hyper-volatile species (CO, CH_4, C_2H_6).

The hyper-volatile carbon monoxide, methane and ethane sublimate at a very low temperatures so they are considered responsible for the outgassing in comets beyond 3 au (Paganini et al. 2013; Bonev et al. 2017), where water ice sublimation is not yet fully activated (CO_2 and O_2 could also play a role if suitably abundant (CO_2/H_2O ~20% in many comets, Ootsubo et al. 2012; O_2/H_2O ~4% in 67P, Bieler et al. 2015)). However, the interesting agreement in the depletion of such volatile species in three disrupting comets could also be a possible indicator of a thermal processing experienced by cometary ices before aggregation. Organic depletion in cometary nuclei could be associated with the formation of cometary ices in a region where the grains are warm enough to allow desorption of hyper-volatile molecules; or it could indicate the degree of thermal or irradiation processing (Willacy et al. 2015).

The formation of methanol on ice grains in the proto-planetary solar nebula is strictly connected to the hydrogenation chemistry of CO-ices. In the generally accepted formative mechanism, CO-ices forms on grain surfaces via direct freeze-out from the gas phase in the molecular cloud, at temperature of about 10 [K]. Subsequently, hydrogenation reactions could increase their chemical complexity before being sequestered by further mantle growth. The chemical pathway starts with the formation of radical HCO, formaldehyde, and ultimately methanol. This chemical path depends strongly on the abundance of H-atoms (and thus on irradiation conditions, to produce H-atoms) and on grain temperatures which controls retention of H-atoms (below about 27K), enabling the methanol abundance ratio to become a signpost of formative conditions of pre-cometary ices. (Charnley & Rodgers 2008; Walsh et al. 2016).

The under-abundant methanol, relative to water, could suggest a formative region for comet E4 (Lovejoy) in which hydrogen-addition reactions were not efficient (perhaps owing to inadequate retention of H-atoms owing to high grain temperatures). Radial mixing of material in the protoplanetary nebula could have exposed transported grains to changing temperatures – inducing a different chemistry whose result delivered the observed comet composition.

Figure 8 reveals a trend of enrichment going from the more volatile species to the less volatile species, observed for the three comets. This is in agreement with an evolutional outgassing scenario in which in-bound comets tend to lose gaseous species according to their sublimation temperatures. This observed enhancement culminates with an over-abundant ammonia and an under-abundant methanol.
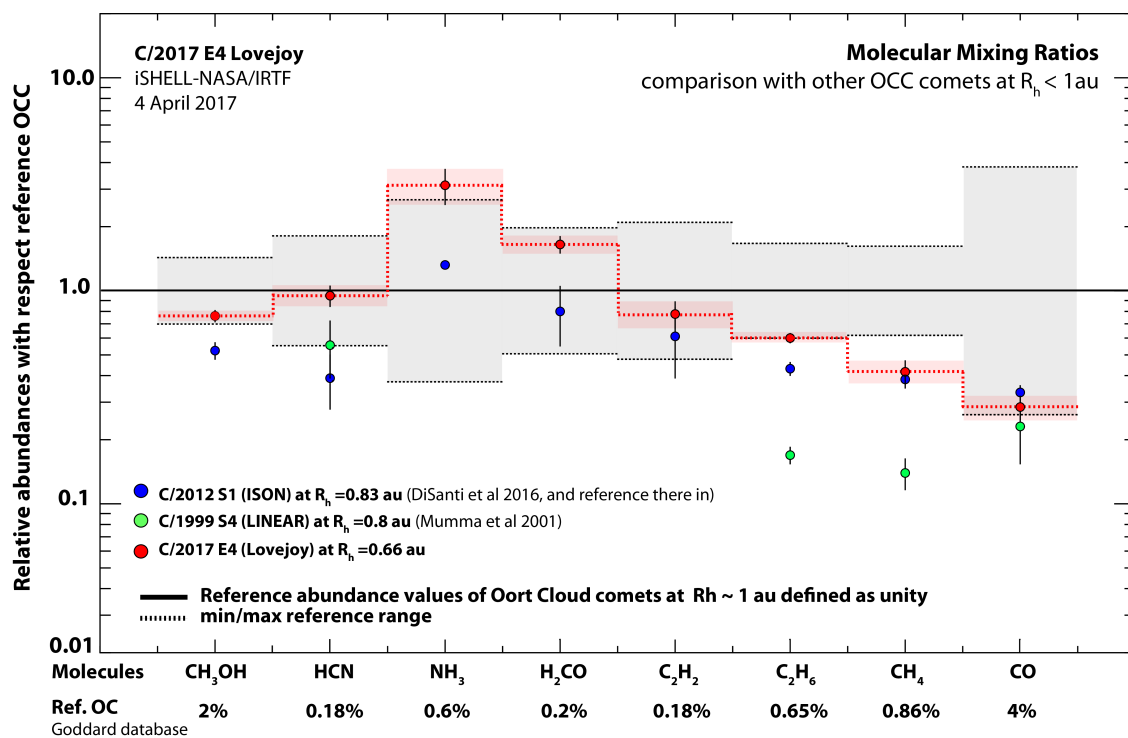
Fig.8 The molecular mixing ratio of comet E4 Lovejoy
The molecular composition of comet E4 Lovejoy is compared with reference values in other Oort cloud comets, and to values in disrupting comets: C/2012 S1 ISON (DiSanti et al. 2016) and comet C/1999 S4 LINEAR (Mumma et al. 2001). The molecular abundances, relative to water, are reported with respect to reference abundance values of Oort Cloud comets. We defined as reference values the median of the values extracted from the copious compilation of values in the Goddard database, and rescaled to unity for each species. In the x-axis the molecular abundance values are reported in the order of volatility from the least-volatile species on the left to the most-volatile species on the right, and below them, the adopted reference abundance values are reported for each species. The grey shadows represent the minimum and maximum reference range. Comet C/2017 E4 Lovejoy organic composition is reported in red circles, dashed lines and red shadows visually enhance our measurements relative to the other comets. The mixing ratio of comet C/2012 ISON is shown in blue while the composition of comet C/1999 S4 LINEAR is reported in green.

4.3 The cometary continuum

The spectrum of a comet is characterized by two components: (1) the continuum (composed of thermal emission from the dust and the nucleus and sunlight reflected from them), and (2) the emission from volatile species. In this section we show the continuum remaining after emission lines of coma gases are subtracted from the measured spectrum of E4. iSHELL is spectrally complete over each order in the L-band, and nearly so in M-band. The combined orders for each band setting provide high accuracy continuous measurements of the spectral energy distribution of comet E4 (Lovejoy) over the range sampled by that instrument setting. The four settings together (L1-c, L3, Lp1-c and M1) sample the range $2.81 - 5.25$ μm in the manner shown in Figure 9. The extracted continuum for each order of iSHELL is shown in circles of four different colors: purple for M1, okra for Lp1, blue for L3 and green for L1. For each order, stochastic error is indicated by vertical lines and the wavelength range of that order by a horizontal line.

The photometric accuracy of our E4 continuum measurements is constrained by systematic uncertainty of the flux standard star, which is defined by atmospheric seeing, imperfect guiding, and slit positioning errors, and not by the stochastic errors evaluated order by order. We evaluated this uncertainty by comparing measured stellar intensities in individual A and B exposures of a nodded ABBA sequence. This error is typically about $\pm 10\%$ for a given setting; all orders within a setting are affected by a common shift, but the relative positions amongst them are not affected. For E4, calibrated data for orders within a setting might shift higher or lower by a common factor but would preserve their relative positions as shown here.

The expected continuum flux density [W/m^2/cm^{-1}] (black full line) of E4 (Lovejoy) was modeled with the Planetary Spectrum Generator (PSG, Villanueva et al. 2018). for comet E4 observing conditions. The code on which PSG is based describes the continuum flux through two simple functions: (1) a Lambertian function to describe the scattered solar black body spectrum and (2) a black body function to describe the dust and nucleus thermal emission component.

Considering that the spectrum of the Sun is known, the model actually describes the overall cometary continuum shape with only one parameter: the temperature of the dust and nucleus (which is assumed to be the same). Four other parameters (the albedo (or reflectivity), the emissivity, the nucleus radius and the gas-to-dust ratio) are used to rescale the flux density to match the predicted and measured spectral flux densities. This simple model does not include any

24

information about the particles size distribution; it provides a simple description of the cometary continuum flux density based on the reflected Solar continuum and the emitted black body of the dust and nucleus. In reproducing the observed continuum of comet E4 (Lovejoy) with PSG, it is not possible to use unique parameters, because real measurements of comet E4 (Lovejoy) nucleus size and albedo, for example, are required to constrain the models. However, assuming typical cometary values, we can offer a reasonable description of the overall spectral energy distribution of the continuum fluxes. Following we present a description of our assumed parameters.

The spatial profile analysis (§3.2) showed that (for individual orders) the dust morphology along the slit is generally in agreement with the molecular outgassing profile, demonstrating that the continuum observed in E4 (Lovejoy) is mainly dominated by reflected sunlight and thermal emission from the dust. The nucleus component is spatially unresolved, so it would show a peaked spatial profile similar to the stellar PSF if present and detected. We assume the dust and gas components have similar column density profiles and thus similar spatial profiles beyond the PSF range, and we assign their difference within the PSF range to a near-nucleus continuum (see Fig. 5a). This nuclear component is not necessarily associated with the nucleus itself; it could be for example explained by the presence of large grains (~mm-cm size) that move slowly in the coma and fragment as they move outward, thence contributing to the small grain continuum. This could also be consistent with a disrupting comet scenario. This near-nucleus residual component, as shown in Figure 5, contributes less than 15-20% to the total flux density within the PSF range.

We assumed a nucleus radius of 500 m, which is the maximum size we can adopt in order to have a dust dominated near-nucleus continuum. The observed comet continuum was then best reproduced by adjusting the temperature to 310 K and the gas-to-dust ratio to 0.8 (see Fig 9). The 5-18 μm color temperature for cometary dust is typically 5-25% higher than a perfect blackbody owing to the inability of sub-micron grains to radiate efficiently. The temperature of a perfect blackbody scales with respect to the heliocentric distance as $T_{bb} = 280 * R_h^{-0.5}$ [K] ; at 0.67 au, T_{bb} is ~ 342 K (for a general review see Kolokolova et al. 2004, and references therein). Contrary to the superheat (359 – 428 K) exhibited by most comets, our best estimate for E4 is 310 K, lower than the blackbody temperature - perhaps suggesting that many grains in the near-nucleus region of this disrupting comet are icy and are thermally limited to colder temperatures by sublimation cooling. It also suggests that the mean grain size in disrupting comet E4 is larger than in most comets on which the mean temperature relation (super-heated) is based.

In reproducing the continuum profile, we adopted a nucleus albedo of 0.06 and an emissivity 0.94; lacking better information, we adopted similar parameters for the dust.

Interestingly, the comet spectral flux density shows two enhanced areas relative to the blackbody model. The first occurs in the wavelength spectral range $3.0 - 3.7$ μm ($\sim 3300 - 2703$ cm^{-1}); the Lp1-c instrument setting ends near 3.7 μm, and the enhanced feature may extend to slightly longer wavelength. Excess emission in the $3.25 - 3.55$ μm was observed in several comet spectra (see Bockelée-Morvan et al. 1995, and references there in): it was first detected in comet 1P/Halley (Tokunaga et al 1987), and later observed in comet 17P/Holmes (Yang et al. 2009). Comet C/2007 W1 Boattini revealed an enhanced feature, but it was not present in comet in 73P/Schwassmann-Wachmann 3-C, (Villanueva et al. 2011b). Recent measurements on come 67P/ Churyumov-Gerasimenko performed with VIRTIS-H showed the appearance of an excess emission feature in the same spectral region associated with outburst activities occurred on 13rd and 14th September 2015 (Bockelée-Morvan et al. 2017).

Generally, this emission feature is associated with several possible origins, either individually or in combination: vibrational stretching of CH bonds in organic molecules, emission features from organic refractory grains, methanol-water ice grains, the combination of several broad ro-vibrational emission bands of methanol, and emission from hydrocarbons, alcohols, or maybe aliphatic and aromatic compounds. However, no unique explanation is offered – either for previous comets or (now) for E4 because it is not trivial to disentangle the gas fluorescent emission from the organic-grain emission.

The second enhanced area falls in the wavelength spectral range $4.5 - 4.8$ μm ($\sim 2222 - 2083$ cm^{-1}), however the short-wavelength limit is defined by the cutoff for the M1 instrument setting and not by the nature of the dust. This enhanced feature could be due to the presence of very small impure water-ice grains, or perhaps to functional groups of complex organic molecules with functional groups such as nitriles (CN $\sim 2220 - 2260$ cm^{-1}) or alkynes ($-C\equiv C-$ $\sim 2100 - 2260$ cm^{-1}). Again, no unique explanation is possible at this writing. A detailed investigation will be explored in a further dedicated paper.
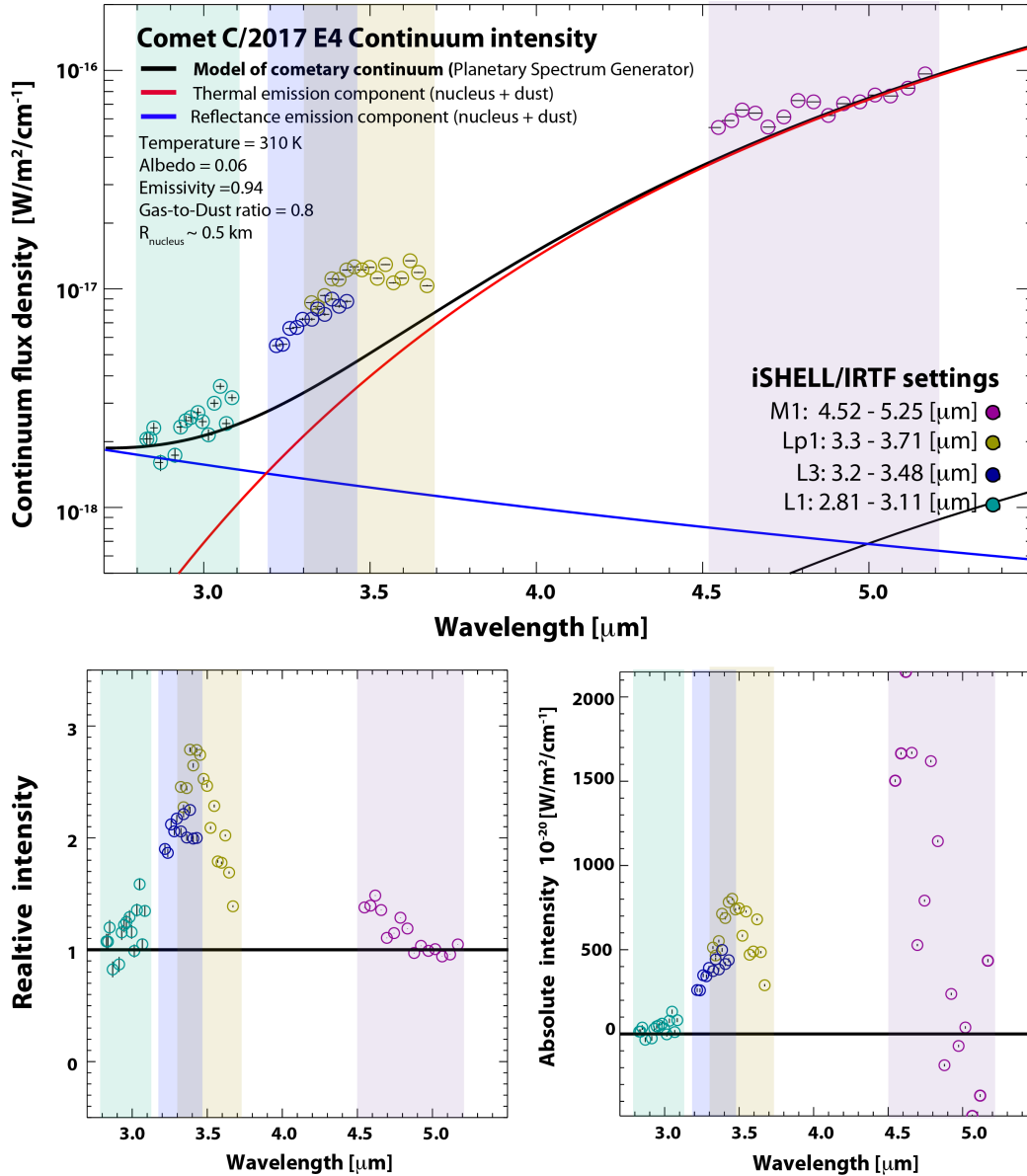
Figure 9. The continuum flux density for Comet C/2017 E4 Lovejoy, with excess emission features noted.
The continuum flux densities measured in each order of iSHELL settings L1-c, L3, Lp1-c and M1 are shown as circles of distinct colors (green, blue, okra, purple), respectively. The boxes with same shade of colors identify the setting ranges. The abscissa is calibrated in wavelength [μm, lower axis] and wavenumber [cm⁻¹, upper axis]. In *Upper Panel:* the continuum flux density [W/m²/cm⁻¹] for each spectral order sampled in the four iSHELL settings is compared with the theoretical continuum intensity (black solid line) estimated using the Planetary Spectrum Generator (Villanueva et al. 2016). The latter is a combination of thermal emission (red solid line) and scattered solar radiation (blue solid line). The model reproduces the overall behavior of the cometary data assuming the comet diameter of 0.5 km, albedo 0.06, temperature of 310 [K], emissivity ε = 0.94 and gas-to-dust ratio 0.8, except for the excesses observed near 3.4 μm and 4.6 μm. *Lower Panels:* Excess emission features are revealed quantitatively by comparing the measured modeled flux densities. In the left panel we divide the measured flux density by the PSG modeled value, order by order, to show the relative excess flux density ratio, while in the right panel we subtract the measured flux density by the PSG modeled value, to show the absolute excess flux density ratio. See text for discussion of confidence limits.

5. Conclusions

Quantitative measurements of the chemical composition of comet E4 (Lovejoy) before its dissolution were presented.

We detected 85 water lines; 58 from setting L1-c in the (2.8 – 3.0) μm range and 27 from setting M1 in the (4.5 – 5.1) μm range. In setting L1-c, lines from eight vibrational water bands were identified, six of which represent non-resonance fluorescence (201-200), (101-001), (200-001), (200-100), (101-100), and (111-110), and two are resonance fluorescence bands (100-000) and (001 – 000). In setting M1, detected water lines belonged to three vibrational water bands; all are in non-resonance fluorescence (100 - 010), (101 – 110), (001-010), and (011-020).

We quantified the nucleus-centered rotational temperatures and water production rates (see Table 2). On 29th-30th March E. Jehin informed us, in a private communication, that production rates for comet E4 were increasing during his previous days of observations. He reported OH production rate around 1.2×10^{28} molecules s^{-1} at Rh = 0.77 au and Delta = 0.61 au; this value is consistent with our nucleus-centered measurements performed on 4 April (reported here, Table 2). After applying seeing corrections and combining measurements from settings L1-c and M1, the global production rate was $(3.16 \pm 0.11) \times 10^{28}$ molecules s^{-1}. The many detected water emission lines enabled accurate retrieval of ortho- and para-H_2O production rates, and thereby reduced systematic uncertainty in the retrieved ortho-para ratio and nuclear spin temperature. The OPR value achieved from the L1-c and M1 settings analyzed together is (2.52 ± 0.09), which corresponds to a spin temperature of $29\,^{+1.55}_{-1.83}$ K.

Molecular production rates and mixing ratios were retrieved for eight more primary volatile species (HCN, NH_3, CO, C_2H_2, C_2H_6, CH_4, CH_3OH, H_2CO) through the four iSHELL settings (L1-c, L3, Lp1-c, and M1). The obtained abundance ratios in E4 (Lovejoy) were compared with reference values of Oort Cloud comets, extracted as the median of values in our infrared database and re-normalized to unity. Results for E4 (Lovejoy) are consistent with median values for most species, excepting methanol (under-abundant) and ammonia (over-abundant) in E4 (Lovejoy). Emission profile analyses showed a general symmetric outgassing morphology, consistent with our observing setup.

The spectrally complete grasp over each order in the L-band and in M-band provided highly accurate measurements of the spectral energy distribution of comet E4 (Lovejoy). The comet

continuum flux density was enhanced in two spectral areas, the first occurs in the wavelength spectral range 3.0 – 3.7 μm (~ 3300 – 2703 cm^{-1}) and the second falls in the wavelength spectral range 4.5 – 4.8 μm (~2222 – 2803 cm^{-1}). Even if no unique explanation is offered at this writing, several possible origins have been discussed to explain such enhanced features, including condensed-phase features and/or the combination of weak lines in several broad ro-vibrational emission bands.

Appendix

Table A.1
Mean flux calibration factors (Γ, coefficients).
Examples of mean flux calibrations factor obtained for few orders in the iSHELL adopted settings.
The complete list of Γ- coefficients obtained for every order is reported as online material.

Order	Frequency [cm^{-1}] [a]	Γ[W/m^2/cm^{-1}/ADU/sec][b]	Throughputs [%][b]
Setting L1-c			
…	…	…	…
174	3352.9076	2.0993E-17	6.06
175	3376.8168	2.1322E-17	5.98
176	3394.2806	2.1578E-17	5.92
177	3412.5216	2.1789E-17	5.85
…	…	…	…
Setting L3			
…	…	…	…
154	2972.8695	1.65592E-17	7.74
155	2991.9625	1.63315E-17	7.85
156	3007.492	1.69475E-17	7.54
157	3032.8125	1.72864E-17	7.44
…	…	…	…
Setting Lp1-c			
…	…	…	…
147	2839.4368	1.33867E-17	9.42
148	2857.9731	1.38271E-17	9.13
149	2877.1585	1.37901E-17	9.15
150	2896.221	1.41043E-17	8.94
…	…	…	…
Setting M1			
…	…	…	…
109	2107.8279	1.1683E-17	10.60
110	2129.2928	1.1642E-17	10.63
111	2129.2928	1.1642E-17	10.63
112	2146.5924	1.1962E-17	10.34
…	…	…	…

[a] Mean frequency across the orders
[b] Mean Γ calibration factors and throughputs of individuals orders

Table A2.
Detected Individual Emission Lines of Volatile Species in C/2017 E4 Lovejoy.
Examples of individual detected water lines characterization.
The complete list of individual detected lines' description for every molecule is presented as online material.

Transition ID up-down	Frequency [cm^{-1}]	Flux TOA ×10^{-19} [W m^{-2}]	g-factor [photons s^{-1} mol^{-1}]	E_{rot} [cm^{-1}]	trn
Water (H$_2$O) *at 81 ± 3 K –* **g-factor ×10^{-8}**					
L1 – *orders 172, 173, 174, 175, 176, 177, 178, 181, 182, 183, 184*					
100.0% ORTHO 201$_{313}$ -200$_{414}$	3329.4180	3.2545 ± 0.6653	1.515	216.31	0.9782
84.7% ORTHO 101$_{313}$ -001$_{422}$	3320.1179	3.9599 ± 0.9063	2.345	333.39	0.9938
100.0% ORTHO 101$_{220}$ -001$_{331}$	3347.9069	4.0573 ± 0.7272	2.780	274.14	0.9889
100.0% ORTHO 201$_{202}$ -200$_{303}$	3346.9917	4.6014 ± 0.7240	3.964	132.09	0.9929
99.9% ORTHO 200$_{312}$ -001$_{413}$	3341.1695	5.5214 ± 0.9479	3.969	271.74	0.9864
100.0% ORTHO 200$_{414}$ -001$_{515}$	3340.9470	4.9293 ± 0.9342	4.088	320.97	0.9840
100.0% ORTHO 200$_{321}$ -001$_{422}$	3339.1156	2.8424 ± 0.8615	1.735	310.19	0.9331
99.7% ORTHO 201$_{211}$ -200$_{312}$	3334.1095	4.0898 ± 0.9571	2.483	167.81	0.9693
		…			
Water (H$_2$O) *at 75 ± 11 K –* **g-factor ×10^{-8}**					
M1 – *orders 101, 104, 105, 108, 109, 111, 112, 113*					
100.0% ORTHO 100$_{414}$ -010$_{505}$	1956.8087	10.625 ± 2.409	8.663	326.02	0.9510
100.0% ORTHO 100$_{110}$ -010$_{221}$	1956.1856	22.782 ± 3.214	37.22	147.56	0.8595
97.5% PARA 100$_{111}$ -010$_{220}$	1949.8073	8.8314 ± 2.0585	12.03	147.54	0.9709
99.1% PARA 100$_{313}$ -010$_{404}$	1979.0886	3.6015 ± 1.9122	6.501	226.15	0.9949
1000% PARA 100$_{202}$ -010$_{313}$	1986.4584	7.4722 ± 1.6930	12.94	144.74	0.9772
100% ORTHO 100$_{303}$ -010$_{312}$	2018.9586	19.810 ± 3.744	18.54	177.67	0.7548
100% ORTHO 100$_{312}$ -010$_{321}$	2008.0575	14.346 ± 2.480	12.45	224.59	0.8637
100% ORTHO 101$_{111}$ -110$_{110}$	2005.0706	2.6936 ± 1.531	3.026	44.69	0.9924
		…			

References

Altwegg, K., Balsiger, H., Bar-Nun, A., et al. 2015, Science, 347, 1261952

Bieler, A., Altwegg, K., Balsiger, H., 2015, Nature 526, Issue 7575, 678

Bockelée-Morvan, D., Woodward, C. E., Kelley, M. S., & Wooden, D. H. 2009, Astrophys J, 696, 1075

Bockelée-Morvan, D., Brooke, T. Y., Crovisier J. 1995, Icarus, 116, 18

Bockelée-Morvan, D., Rinaldi, G., Erard, S., et al., 2017 MNRS 469, S443

Bonev, B. P. 2005, Towards a Chemical Taxonomy of Comets: Infrared Spectroscopic Methods for Quantitative Measurements of Cometary Water (The University of Toledo: Ph.D. Thesis), 322

Bonev, B. P., Mumma, M. J., Kawakita, H., Kobayashi, H., & Villanueva, G. L. 2008, Icarus, 196, 241

Bonev, B. P., Villanueva, G. L., DiSanti, M. A., et al. 2017, Astron J, 153, 241

Bonev, B. P., Villanueva, G. L., Paganini, L., et al. 2013, Icarus, 222, 740

Buntkowsky, G., Limbach, H. H., et al. 2008, Zeitschrift für Physikalische Chemie 222, 1049

Charnley, S. B., & Rodgers, S. D. 2008, Space Sci Rev, 138, 59

Combes, M., Moroz, V. I., Crifo, J. F., et al. 1986, Soviet AstrLett (TR:PISMA) V12, 12, 257

Crovisier, J. 1997, Science, 275, 1904

Crovisier J, Encrenaz Th, Lellouch E, Bockelée-Morvan D, Altieri B, et al. 1999, In *The Universe as Seen by ISO*, ed. P Cox, MF Kessler, ESA-SP 427:161. Noordwijk, Neth.: ESA

Dello Russo, N., Bonev, B. P., DiSanti, M. A., et al. 2005, Astrophys J, 621, 537

Dello Russo, N., DiSanti, M. A., Mumma, M. J., Magee-Sauer, K., & Rettig, T. W. 1998, Icarus, 135, 377

Dello Russo, N., Mumma, M. J., DiSanti, M. A., et al. 2006, Icarus, 184, 255

DiSanti, M. A., Bonev, B. P., Gibb, E. L., et al. 2016, Astrophys J, 820, 34

DiSanti, M. A., Bonev, B. P., Magee-Sauer, K., et al. 2006, Astrophys J, 650, 470

DiSanti, M. A., Villanueva, G. L., Paganini, L., et al. 2014, Icarus, 228, 167

Eberhardt, P., Reber, M., Krankowsky, D., & Hodges, R. R. 1995, A&A, 302, 301

Faggi, S., Villanueva, G. L., Mumma, M. J., et al. 2016, Astrophys J, 830, 157

Faggi, S., Villanueva, G. L., & Mumma, M. J. 2017, https://psg.gsfc.nasa.gov/apps/ishell.php

Gelaro, R., McCarty, W., Suarez, M. J., et al. 2017, J Climate, 30, 5419

Hama, T., & Watanabe, N. 2013, Chemical Reviews, 113, 8783

Hama, T., Watanabe, N., et al. 2011, Astrophys J, 738, L15

Hase, F., Demoulin, P., Sauval, A. J., et al. 2006, J Quant Spectrosc Radiat Transfer, 102, 450

Jessberger, E. K., Christoforidis, A., & Kissel, J. 1988, Nature, 332, 691

Kawakita, H., Dello Russo, N., Furusho, R., et al. 2006, Astrophys J, 643, 1337

Kawakita, H., Kobayashi, H., & Kobayashi, H. 2009, Astrophys J, 693, 388

Kolokolova et al. 2004 (Comets II)

Larson, H. P., Davis, D. S., Mumma, M. J., & Weaver, H. A. 1986, Ap. J. 309, L95

Levison, H. F., Morbidelli, A., Tsiganis, K., Nesvorný, D., & Gomes, R. 2011, Astron J, 142, 152

Morbidelli, A. 2005, arXiv.org, Vol. astro-ph

Morbidelli, A., & Rickman, H. 2015, A&A, 583, A43

Morbidelli, A., Chambers, J., Lunine, J. I., et al. 2000, Meteoritics & Planetary Science, 35, 1309

Mumma, M. J., & Charnley, S. B. 2011, Ann. Rev. Astron. Astrophys. 49:471

Mumma, M. J., Blass, W. E., Weaver, H. A., & Larson, H. P. 1988, BAAS, 20, 826

Mumma, M. J., Dello Russo, N., DiSanti, M. A., et al. 2001, Science, 292, 1334

Mumma, M. J., DiSanti, M. A., Dello Russo, N., et al. 2003, Adv Space Res, 31, 2563

Mumma, M. J., Weaver, H. A., Larson, H. P., et al. 1986, Science, 232, 1523

Mumma, M. J., Weaver, H. A., & Larson, H. P. 1987, Astron & Astrophy 187, 419

Mumma, M. J., Weissmann, P. R., Stern, S. A., 1993
      "Comest and the Origin of the Solar System: Reading the Rosetta Stone", in Protostars
      and Planets III, Univ. of Ariz. Press, pp. 1177-1252.

Ootsubo, T., Kawakita, H.,Hamada, S. 2012, Astrophys J, 752, 15

Paganini, L., DiSanti, M. A., Mumma, M. J., et al. 2014, Astron J, 147, 15

Paganini, L., Mumma, M. J., Bonev, B. P., et al. 2012, Icarus, 218, 644

Paganini, L., Mumma, M. J., Villanueva, G. L., DiSanti, M. A., & Bonev, B. P. 2015, Astrophys
      J, 808, 1

Paganini, L., Mumma, M. J., Boehnardt, H., et al. 2013, Astrophys J, 766, 100

Paganini, L., Mumma, M., Villanueva, G., et al. 2014b, Asteroids

Rayner, J., Bond, T., Bonnet, M., et al. 2012, eds. I. S. McLean, S. K. Ramsay, & H. Takami,
      Vol. 8446 (SPIE), 84462C

Shinnaka, Y., Kawakita, H., et al. 2011, Astrophys J, 729, 81

Sliter, R., Gish, M., et al. 2011, J Phys Chem A, 115, 34, 9682

Tokunaga, A. T., Nagata, T., Smith, R. G. 1987 Astron & Astrophy, 187, 519

Villanueva, G. L., DiSanti, M. A., Mumma, M. J., Xu, L.-H., & Xu, L.-H. 2012a, Astrophys J,
      747, 1

Villanueva, G. L., Magee-Sauer, K., & Mumma, M. J. 2013b, J Quant Spectrosc Rad Transfer,
      129, 158

Villanueva, G. L., Mumma, M. J., & Magee-Sauer, K. 2011a, J Geophys Res Pl, 116, 1

Villanueva, G. L., Mumma, M. J., Bonev, B. P., et al. 2012b, J Quant Spectrosc Radiat Transfer,
      113, 202

Villanueva, G. L., Mumma, M. J., DiSanti, M. A., et al. 2011b, Icarus, 216, 227

Villanueva, G. L., Smith, M., Protopapa, S., Faggi, S., Mandell, A. M. 2018, J Quant Spectrosc
      Rad Transfer, 217, 86-104

Villanueva, G. L., Mumma, M. J., Novak, R. E., & Hewagama, T. 2008, J Quant Spectrosc
      Radiat Transfer, 109, 883

Villanueva, G. L., Mumma, M. J., Novak, R. E., et al. 2013a, Icarus, 223, 11

Walsh, C., Loomis, R. A., Oberg, K. I., et al. 2016, arXiv.org, Vol. astro-ph.EP, L10

Weaver, H. A., Mumma, M. J., Larson, H. P., & Davis, D. S. 1986, Nature, 324, 441

Willacy, K., Alexander, C., Ali-Dib, M., et al. 2015, arXiv.org, Vol. astro-ph.EP (Springer
      Netherlands), 151

Wilson, T. G., Rawlings, J. M. C., & Swinyard, B. M. 2017, Mon Not R Astron Soc, 466, 1954

Woodward, C. E., Kelley, M. S., Bockelée-Morvan, D., & Gehrz, R. D. 2007, Astrophys J, 671,
      1065

Xie, X., & Mumma, M. J. 1996, Astrophys J, 464, 457

Yamamoto, T. 1985, A&A, 142, 31

Yang, B., Jewitt, D. Bus, S. J. 2009, Astrophys J, 137, 4538